

# Charge-transfer and Mott-Hubbard Excitations in FeBO<sub>3</sub>: Fe K edge Resonant Inelastic X-ray Scattering Study

Jungho Kim\* and Yuri Shvyd'ko†

Advanced Photon Source, Argonne National Laboratory, Argonne, Illinois 60439, USA

(Dated: May 29, 2018)

*Momentum-resolved* resonant inelastic x-ray scattering (RIXS) spectroscopy has been carried out at the Fe K edge, successfully for the first time. The RIXS spectra of a FeBO<sub>3</sub> single crystal reveal a wealth of information on  $\simeq 1 - 10$  eV electronic excitations. The IXS signal resonates both when the incident photon energy approaches the pre-edge ( $1s-3d$ ) and the main-edge ( $1s-4p$ ) of the Fe K edge absorption spectrum. The RIXS spectra measured at the pre-edge and the main-edge show quantitatively different dependences on the incident photon energy, momentum transfer, polarization, and temperature. Electronic excitations observed in the pre-edge and main-edge RIXS spectra are interpreted as Mott-Hubbard (MH) and charge-transfer (CT) excitations, respectively. The charge-transfer gap  $\Delta_G = 3.81 \pm 0.04$  eV and the Mott-Hubbard gap  $U_G = 3.96 \pm 0.04$  eV, are determined, model independently from the experimental data. The CT and MH excitations are assigned using molecular orbitals (MO) in the cluster model and multiplet calculation in the many-electron multiband model, respectively.

PACS numbers: 78.70.En, 71.20.Be, 78.20.-e, 75.50.Ee

## I. INTRODUCTION

Iron borate, FeBO<sub>3</sub> is a classical material with strong electron correlations experiencing interesting magnetic, optical, and magneto-optical properties. A review of the early studies on crystal growth, structure, physical properties (magnetic, elastic, magnetoelastic, optical, and magneto-optical) and applications of FeBO<sub>3</sub> can be found in Ref. 1. It is among only a few known materials magnetically ordered at room temperature and transparent in the visible spectrum,<sup>2,3</sup> making FeBO<sub>3</sub> attractive in applications for broadband visible magneto-optical devices. A number of electronic and magnetic phase transitions induced by high pressure have been observed recently: collapse of the magnetic moment of Fe<sup>3+</sup> ions,<sup>4,5</sup> insulator-semiconductor transition,<sup>6,7</sup> increase of the Néel temperature.<sup>8</sup> The driving mechanism for these high-pressure phenomena is attributed to the electronic transition in Fe<sup>3+</sup> ions from the high-spin  $3d^5$  ( $S = 5/2$ ,  $^6A_{1g}$ ) to the low-spin ( $S = 1/2$ ,  $^2T_{2g}$ ) state (spin crossover).<sup>8,9</sup>

Despite a great number of experimental and theoretical studies that have been performed, the electronic structure of FeBO<sub>3</sub> is still not completely understood. Ovchinnikov and Zabluda<sup>10</sup> developed an empirical many-electron model that took all  $d$  orbitals into account and strong electron correlations involving  $d$  electrons of Fe atoms. The magnitude of the main parameters of the band structure, such as the charge-transfer (CT) gap  $\Delta_G$ , Mott-Hubbard (MH) gap  $U_G$ , crystal-field splitting  $10Dq$ , etc., are derived from optical absorption spectra and x-ray photoemission spectroscopy.<sup>7,10</sup> The same scheme has been applied to interpret high pressure induced magnetic collapse and insulator-metal transition.<sup>9</sup> The first-principles local-density approximation (LDA) energy band calculations predicted an antiferromagnetic (AFM) metal instead of an AFM insulator.<sup>11</sup> Shang

*et al.*<sup>12</sup> have performed first-principles band-structure calculations using the density functional theory within the generalized gradient approximation (GGA) and the GGA+U approach. The electronic structure was predicted to be high-spin, antiferromagnetic and insulating, in agreement with experiments. However, in order to predict the correct value of the bandgap in the first-principle calculation, the Coulomb repulsion  $U = 7$  eV has to be assumed, much higher than  $U = 2.97$  eV obtained in the empirical many-electron model of Ref. 10.

An insulating ground state in a transition metal (TM) compound is realized by an on-site  $U$ , giving rise to the split of the conduction band into lower and upper Hubbard bands (LHB and UHB, respectively). If  $U$  is small, the insulating charge gap arises from the MH excitation between LHB and UHB. On the other hand, when  $U$  is quite large, the insulating charge gap arises from the CT excitation between the highest occupied ligand ( $O 2p$ ) and UHB. In the Zaanen-Sawatzky-Allen (ZSA) scheme,<sup>13</sup> the TM compound is classified as a MH type in the first case and a CT type in the second case. The general trend is that early TM compounds belong to the MH type and late TM compounds, such as cuprates, belong to the CT type. For Fe compounds with half-filled ( $d^5$ ), such as FeBO<sub>3</sub>, however, the classification is not as clear;  $U_G$  from the lowest MH excitation is comparable with  $\Delta_G$  from the lowest CT excitation.

Probing CT and MH excitations is important to resolve the existing ambiguities in determination of the electronic structure and parameters in FeBO<sub>3</sub>. Conventional spectroscopy, such as optical spectroscopy, is of limited utility; it has difficulty in probing dipole-forbidden charge excitation, such as MH excitation, and characterization of probed charge excitation is not straightforward because it cannot probe CT and MH excitations selectively. A higher order spectroscopy that uses the excited electronic state of interest as an intermediate state can pro-

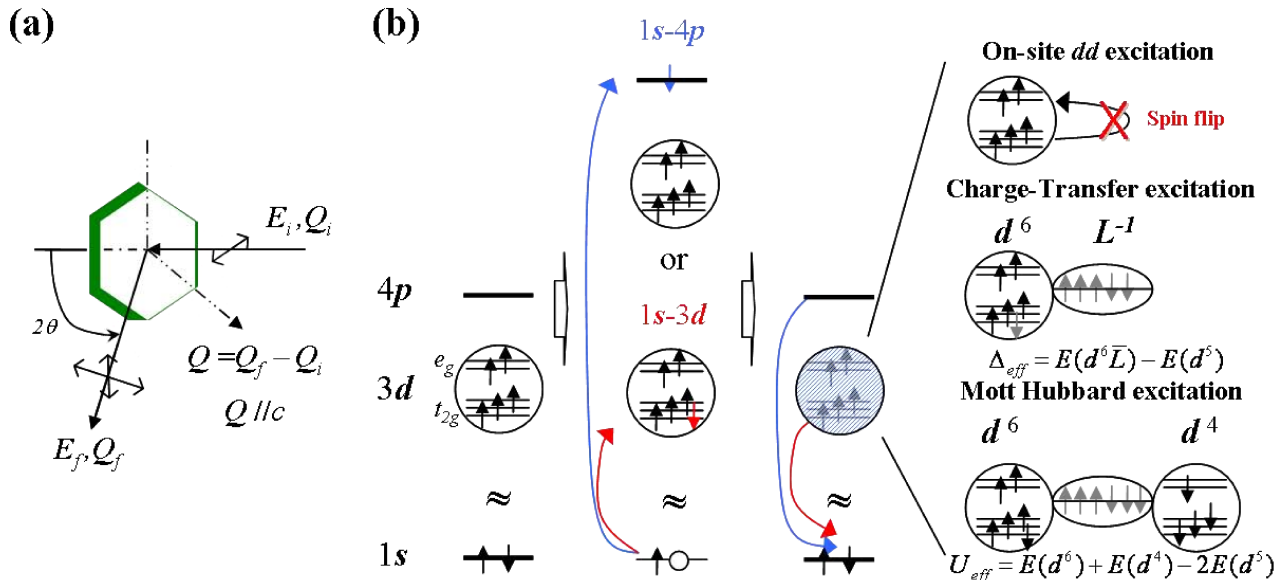


FIG. 1: (a) Schematic of the RIXS experiment in the horizontal scattering geometry, where the incident photon polarization is parallel to the scattering plane ( $\pi$ -polarization). The FeBO<sub>3</sub> sample is mounted in a way that the momentum transfer  $Q = Q_f - Q_i$  is along the crystal  $c$  axis. The scattered photon energy is measured by a spectrometer consisting of a Ge(620) spherical diced analyzer and a position-sensitive micro strip detector. (b) Schematic of a Fe K edge RIXS process in FeBO<sub>3</sub>. In the initial state, five 3d electrons fill  $t_{2g}$  and  $e_g$  crystal-field levels in the high spin configuration. Two distinct absorption transitions can be used for RIXS measurement: the pre-edge ( $1s-3d$ ) and the main-edge ( $1s-4p$ ) of the Fe K edge absorption spectrum. Various valence electronic excitations are left after the decay of the excited electron back into the 1s core level: on-site  $dd$ , charge-transfer, and Mott-Hubbard excitations. On-site  $dd$  excitations are forbidden because they require spin-flip.

vide a way to circumvent the limitation.

Momentum-resolved resonant inelastic x-ray scattering (RIXS) at the K edge plays an increasingly important role as a photon-in photon-out higher order spectroscopic tool for investigation of localized and propagating charge excitations in TM compounds providing bulk-sensitive, element-specific information. A variety of systems, including cuprates,<sup>14–20</sup> manganites,<sup>21,22</sup> and nickelates,<sup>23,24</sup> have been studied by RIXS. Charge excitations probed by RIXS are known to strongly depend on the RIXS intermediate excited state. The CT excitations are usually observed in cuprates by K edge RIXS.<sup>15–18,20,23,25,26</sup> On the other hand, on-site  $dd$  excitations of cuprates can be probed by RIXS at Cu  $M_{2,3}$ -<sup>27</sup> and  $L_3$ -edge,<sup>28</sup> which involves direct transitions to and from 3d states.

It is well known that there exist two distinct transitions in the Fe K edge: the pre-edge  $1s-3d$  and the main-edge  $1s-4p$  where the underline denotes a hole. While the latter is dipole allowed, the former  $1s-3d$  transition is quadrupole allowed or particularly dipole allowed when static or dynamic local distortions exist. The  $1s-3d$  absorption would show up as a weak peak, just below the strong  $1s-4p$  absorption peak. This pre-edge ( $1s-3d$ ) can be used for the resonant enhancement of an inelastic x-ray scattering (IXS) signal. The pre-edge RIXS enables direct access to the 3d valence system, similar to the M edge ( $3p-3d$ ) or the L edge ( $2p-3d$ ) RIXS<sup>29</sup> but without

a complexity imposed by the spin-orbit interaction.

Figure 1(b) shows a schematic diagram of the Fe K edge RIXS process in FeBO<sub>3</sub>. In the initial state, five 3d electrons fill  $t_{2g}$  and  $e_g$  crystal-field levels in the high-spin configuration. As a first step, the 1s core electron is excited to 3d (pre-edge) or 4p (main-edge), the excited electron decays back into the 1s core level creating various charge excitations with an energy  $\varepsilon$  equal to the energy loss of the incident photon  $\varepsilon = E_i - E_f$ . Measuring RIXS spectra  $S(\varepsilon, Q, E_i)$  for a given momentum transfer  $Q = Q_f - Q_i$  provides valuable information on charge excitations in solids. The availability of two absorption transitions at the K edge provide an opportunity to probe charge excitations selectively. One can assume that the on-site  $dd$  and MH excitations could be better observed in the pre-edge RIXS than the main-edge RIXS, because an intermediate state of the pre-edge RIXS directly involves 3d states. However, until now this has not been demonstrated.

In the present study, we explore this possibility by measuring RIXS spectra using both intermediate states. We will refer to the pre-edge RIXS when the incident photon energy is tuned to the energy of the  $1s-3d$  ( $E_i \approx 7113.5$  eV) transition. Similarly, we will refer to the main-edge RIXS if the incident photon energy is tuned to the energy of the  $1s-4p$  ( $E_i \approx 7131$  eV) transition. In the following sections, we will present the pre-edge and main-edge RIXS spectra in FeBO<sub>3</sub> measured as a

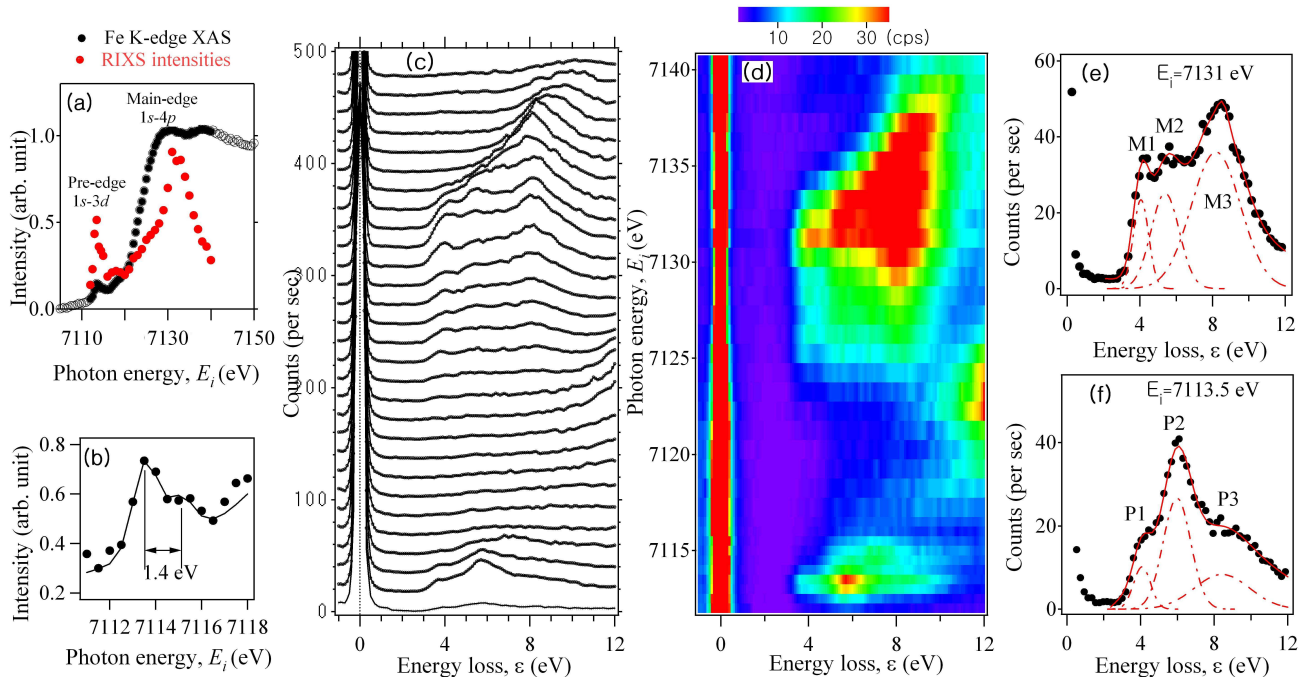


FIG. 2: (a) Fe K edge x-ray absorption spectrum (XAS) of  $\text{FeBO}_3$  measured in PFY mode (black open dots) and integrated intensities of the RIXS spectra of (c) (red filled dots). (b) XAS same as in (a) but shown on the expanded scale of  $E_i$  around the pre-edge. (c) RIXS spectra measured for different incident photon energies  $7112 \text{ eV} \leq E_i \leq 7140 \text{ eV}$ . (d) 2D plot of the RIXS spectra of (c). (e) and (f) show representative RIXS spectra of the main-edge RIXS ( $E_i=7131 \text{ eV}$ ,  $Q=(0 \ 0 \ 9)$ ) and the pre-edge RIXS ( $E_i=7113.5 \text{ eV}$ ,  $Q=(0 \ 0 \ 9)$ ), respectively. Gaussian functions are used to fit inelastic peaks, while the Voigt function is used to fit the elastic line (see the text).

function of the excitation energy, momentum transfer, polarization, and temperature. We show that unlike previously studied cases, the K edge RIXS can probe both CT and MH excitations at the same time. We interpret the pre-edge and the main-edge RIXS excitations as MH and CT excitations, respectively, and derive important quantities including the charge-transfer gap  $\Delta_C$  and the Mott-Hubbard gap  $U_C$  using molecular orbitals (MO) in the cluster model and multiplet calculation in the many-electron multiband model. This study demonstrates a special quality of the K edge RIXS to be a simultaneous probe of CT and MH excitations in TM compounds.

## II. EXPERIMENT AND SAMPLE

The RIXS measurements were performed using the MERIX spectrometer at the XOR-IXS 30-ID beamline of the Advanced Photon Source (APS). The sample is mounted in the Displex closed-cycle cryostat NE-202N with a temperature range of 6 K to 450 K. The measurements were carried out at room temperature and at temperatures close to the Néel temperature ( $T_N=348 \text{ K}$ ). X-rays impinging upon the sample were monochromatized to a bandwidth of 75 meV, using a four-bounce (+ - - +) monochromator with asymmetrically cut Si(400) crystals.<sup>30</sup> The beam size on the crystal was reduced to

$45(\text{H}) \times 20(\text{V}) \mu\text{m}^2$  by focusing in the Kirkpatrick-Baez configuration. The photon flux on the sample was  $1.1 \times 10^{12} \text{ ph/s}$ . The total energy resolution of the MERIX spectrometer at the Fe K edge is 180 meV. This is achieved using a Ge(620) spherical diced analyzer, and a position-sensitive microstrip detector placed on a Rowland circle with a 1 m radius. The silicon microstrip detector with 125  $\mu\text{m}$  pitch is applied for the purpose of reducing the geometrical broadening of the spectral resolution function.<sup>31</sup> Maximum RIXS count rates were in the range of 40-50 Hz. Horizontal scattering geometry, where the incident photon polarization vector component is parallel to the scattering plane ( $\pi$ -polarization), was used for all RIXS measurements, with the crystal  $\mathbf{c}$ -axis in the scattering plane as shown in Fig. 1(a).

Iron borate,  $\text{FeBO}_3$ , single crystal with low-dislocation density, grown by spontaneous crystallization from flux,<sup>32</sup> was used in the current experiment. The crystal has a form of a platelet  $6 \times 7 \times 0.15 \text{ mm}^3$ , with  $\mathbf{c}$ -axis perpendicular to the platelet surface. Iron borate has a rhombohedral calcite structure that belongs to the space group  $R\bar{3}c(D_{3d}^6)$  with two formula units per unit cell. The lattice constants are  $\mathbf{a}=\mathbf{b}=4.626(1) \text{ \AA}$  and  $\mathbf{c}=14.493(6) \text{ \AA}$ . The  $\text{Fe}^{3+}$  ions are centered in a slightly distorted  $O_6^{2+}$  octahedra. The octahedral  $O_h$  crystal field splits the energy of the 3d orbitals into three-fold degenerate  $t_{2g}$  and two-fold degenerate  $e_g$  states. As depicted

in Fig. 1(b), five  $3d$  electrons fill these crystal-field levels in the high-spin configuration.<sup>5</sup>  $\text{FeBO}_3$  is a large-gap antiferromagnetic insulator with the Néel temperature  $T_N=348$  K below which the two sublattice magnetic moments along the  $\mathbf{c}$ -axis order antiferromagnetically. All of the  $\text{Fe}^{3+}$  spins are in the plane perpendicular to the  $\mathbf{c}$ -axis. Nearest-neighbor (NN) exchange interaction of the  $\text{Fe}^{3+}$  spins is antiferromagnetic. A slight canting of two sublattice magnetic moments gives rise to a weak ferromagnetic moment.

### III. DATA AND ANALYSIS

#### A. Incident photon energy ( $E_i$ ) dependence

Figure 2(a) presents Fe K edge x-ray absorption spectra (XAS) of  $\text{FeBO}_3$ , measured in the partial fluorescence yield (PFY) mode, by detecting Fe  $K_\alpha$  fluorescence. A strong absorption main-edge ( $1s-4p$ ) around 7130 eV and a weak absorption pre-edge ( $1s-3d$ ) around 7114 eV are observed. Figure 2(b) shows the pre-edge XAS on the expanded energy scale. A fine structure with two peaks can be resolved. The peak separation is estimated to be 1.4 eV. In the strong crystal field limit, two peaks are assigned to  $1s-3d(t_{2g})$  and  $1s-3d(e_g)$  transitions. The peak separation corresponds to the crystal-field splitting,  $10Dq=1.4$  eV.<sup>33</sup>

The RIXS spectra have been measured at  $\mathbf{Q}=(0\ 0\ 9)$  with  $E_i$  changing from the pre-edge to the main-edge absorption energies indicated by filled black circles in Fig. 2(a). Figure 2(c) shows RIXS spectra measured as a function of the energy loss ( $\varepsilon$ ) with 1 eV increment in  $E_i$ . Every spectrum shows a strong elastic signal at  $\varepsilon=0$ . The RIXS signal resonates around  $E_i=7131$  eV and  $E_i=7113.5$  eV. The 12 eV feature in the RIXS spectra observed for  $E_i$  between main-edge and pre-edge RIXS is due to the  $K\beta_5$  emission. Intensities of the RIXS spectra integrated in the range  $2\text{ eV} \leq \varepsilon \leq 12\text{ eV}$  are plotted in Fig. 2(a). The two resonances are clearly seen.

Figure 2(d) shows a 2D plot of RIXS intensities in ( $E_i, \varepsilon$ ) space. That there is a difference in resonance dependence for the main-edge and the pre-edge RIXS is easily seen. The 2D color plot in the main-edge RIXS region shows a typical  $E_i$  dependence observed in a number of previously reported main-edge RIXS studies on cuprates:<sup>14,25,34</sup> the intensity of the 4 eV and 6 eV features drops rapidly as  $E_i$  increases from 7131 eV. Such resonance behavior is often explained by the third-order perturbation theory, where the RIXS cross section can be factorized into a resonant prefactor that depends on the incident and scattered photon energies and dynamic structure factor.<sup>14,25,26,34,35</sup> In contrast, the shape of the pre-edge RIXS spectrum is stable with respect to change in  $E_i$ . A similar  $E_i$  dependence is observed in the L edge ( $2p-3d$ ) RIXS<sup>36</sup> and the Ni pre-edge ( $1s-3d$ ) RIXS in NiO, in which the on-site  $dd$  excitations are probed. This observation suggests that the features in the pre-edge RIXS

spectrum undergo the same RIXS process as with  $dd$  excitations, which occur in the direct transition to and from the  $3d$  states and are well described by the second-order perturbation theory (Kramers-Heisenberg equation).

The RIXS spectra show no low-energy feature with  $\varepsilon < 3$  eV. This is the region where on-site  $dd$  excitation should take place. On-site  $dd$  excitations in  $\text{FeBO}_3$  are forbidden when five  $3d$  electrons of  $\text{FeBO}_3$  are in the high-spin configuration as shown in Fig. 1(b). This observation proves that RIXS does not probe charge excitation accompanied by spin-flip.

Figures 2(e) and (f) show representative RIXS spectra corresponding to the main-edge ( $E_i=7131$  eV) and the pre-edge ( $E_i=7113.5$  eV) RIXS, respectively. In order to obtain quantitative information on the peak positions and their intensities, Gaussian functions are used to fit inelastic peaks while the Voigt function is used to fit the elastic peak. Note that the influence of elastic tail intensity on the inelastic intensity is marginal because the inelastic peaks are pretty far away from the elastic peak. For the main-edge RIXS spectra, three peaks could be identified at around 4.09 eV (M1), 5.29 eV (M2), and 8.14 eV (M3). The pre-edge RIXS spectra show different high-energy features: a small shoulder peak at around 3.96 eV (P1), a strong main peak at around 5.85 eV (P2) peak, and a broad peak at around 8.71 eV (P3).

#### B. Momentum transfer dependence

Momentum transfer ( $\mathbf{Q}$ ) dependence of the RIXS spectrum provides valuable information on the dispersion of the occupied and unoccupied bands.<sup>37</sup> In this section, we present  $\mathbf{Q}$  dependences of the observed RIXS spectra measured along the  $\mathbf{c}$ -axis:  $\mathbf{Q} = (0\ 0\ L)$ .

Figures 3(a) and (b) show the main-edge RIXS spectra measured for different  $\mathbf{Q}$ . The scattering angle  $2\theta$  of the bottom and the top spectra in Fig. 3(a) are about  $14^\circ$  ( $L \cong 2$ ) and  $92^\circ$  ( $L \cong 11.5$ ), respectively. Noticeable changes with  $\mathbf{Q}$  are observed in peak positions and intensities. The M1 and M2 peaks disperse shifting to lower energy as  $\mathbf{Q}$  approaches  $(0\ 0\ 6)$  and moving back to higher energy as  $\mathbf{Q}$  increases further. The RIXS intensity decreases for  $L > 6$  as shown in Fig. 3(b). Let us discuss first the  $\mathbf{Q}$  dependence of the peak positions. The peak intensity changes will be discussed later.

The positions of M1 and M2 peaks are shown as a function of  $\mathbf{Q}$  in Fig. 3(e). Peak M1 is located at around 4.09 eV for  $\mathbf{Q}=(0\ 0\ 1.9)$ . As  $\mathbf{Q}$  approaches  $(0\ 0\ 6)$ , the peak energy changes to  $3.81 \pm 0.04$  eV. With a further increase of  $\mathbf{Q}$  to  $(0\ 0\ 9)$ , M1 moves back to the higher energy of  $4.09 \pm 0.07$  eV. Although it is not evident from the raw data of Fig. 3(a) and (b), due to a small RIXS intensity at  $L > 9$ , the results from the numerical data evaluation shown in Fig. 3(e) demonstrate that M1 again disperses to the lower energy of  $3.86 \pm 0.10$  eV as  $\mathbf{Q}$  approaches  $(0\ 0\ 12)$ . The dispersion width of the M1 peak is about 0.26 eV. The M2 peak shows the same dispersion

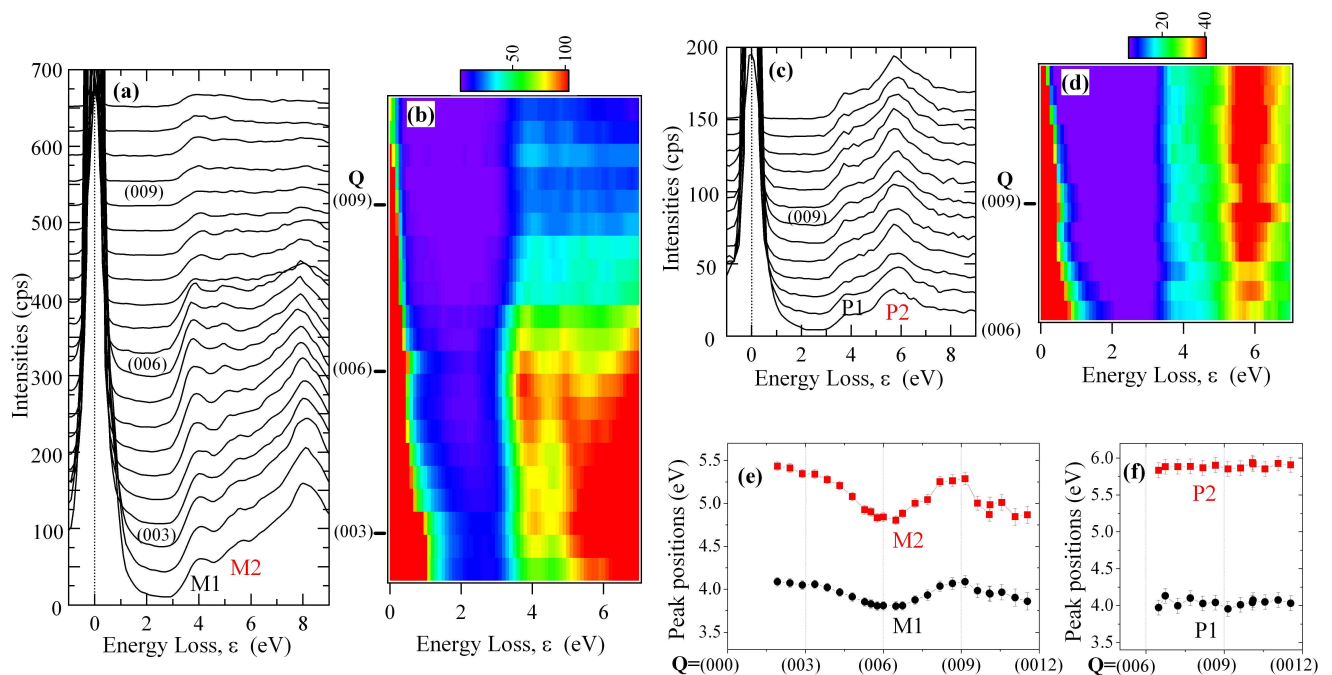


FIG. 3: RIXS spectra measured at the (a) main-edge, and (c) pre-edge as function of  $\mathbf{Q} = (0\ 0\ L)$ ,  $2 < L < 11.5$ . 2D plots of the corresponding RIXS data are shown in (b) and (d), respectively. (e)  $\mathbf{Q}$  dependence of the M1 and M2 peaks derived from RIXS spectra in (a). (f)  $\mathbf{Q}$  dependence of the P1 and P2 peaks from RIXS spectra in (c).

behavior but with a larger dispersion width of  $0.44\text{ eV}$ :  $4.84 \pm 0.04\text{ eV}$  at  $\mathbf{Q}=(0\ 0\ 6)$ ,  $5.29 \pm 0.07\text{ eV}$  at  $\mathbf{Q}=(0\ 0\ 9)$ , and  $4.87 \pm 0.10\text{ eV}$  at  $\mathbf{Q}=(0\ 0\ 12)$ . Note that  $\mathbf{Q}=(0\ 0\ 6)$  corresponds to the first allowed Bragg reflection along this highly symmetric direction and  $(0\ 0\ 12)$  is the second one. Therefore, these two low-lying excitations have the normal dispersion relation showing direct energy gaps. The mean energy difference between these two low-lying peaks is  $1.13 \pm 0.13\text{ eV}$ .

Figures 3(c) and (d) show the pre-edge RIXS spectra measured for different  $\mathbf{Q} = (0\ 0\ L)$ . The  $2\theta$  values of the bottom and the top spectra in Fig. 3(c) are about  $48^\circ$  ( $L \cong 6.5$ ) and  $92^\circ$  ( $L \cong 11.5$ ), respectively. Contrary to the M1 and M2 peaks in the main-edge RIXS spectra, the P1 and P2 peaks do not show any noticeable peak intensity and position changes. The positions of P1 and P2 are shown in Fig. 3(f). As mentioned above, the peak positions are stable. The mean energy is  $3.96 \pm 0.05\text{ eV}$  and  $5.85 \pm 0.03\text{ eV}$  for M1 and M2, respectively. The mean energy difference between these two low-lying peaks is  $1.85 \pm 0.04\text{ eV}$ .

The dispersive nature of charge excitation has been reported for a CT excitation of cuprates in a number of RIXS studies.<sup>15,16,20,23,38,39</sup> The CT excitation in cuprates is defined as the excitation from the Zhang-Rice band ( $O\ 2p$ ) to the upper Hubbard band (UHB). For example, the  $2\text{ eV}$  peak of  $\text{La}_2\text{CuO}_4$  which is assigned as the CT excitation, shows a sizable dispersion of  $0.1\sim 0.5\text{ eV}$ .<sup>20,23,39</sup> On the other hand, it has been reported that Mott-Hubbard (MH) excitations in manganites do not show any obvious dispersive behavior.<sup>21,22,40</sup>

The MH excitation in manganites is defined as the excitation from the lower Hubbard band (LHB) to the UHB. The dispersive behavior of the CT excitations and non dispersive behavior of the MH excitation can be attributed to the fact that, in general, the delocalized ligand  $2p$  band has a larger bandwidth than the transition metal  $3d$  band.

Using this analogy, the charge excitations probed by the main-edge and pre-edge RIXS can be attributed to CT and MH excitations, respectively. In these assignments, the dispersion of the main-edge RIXS excitation is understood as resulting from the dispersive occupied oxygen  $2p$  band and the dispersive UHB, while no dispersion of the pre-edge RIXS excitation is attributed to the non dispersive LHB.

### C. Photon polarization dependence

The intensity of the RIXS features vary with  $\mathbf{Q}$  or equivalent scattering angle. This can be attributed to the photon polarization dependence of the RIXS cross section. In our experiment, the incident photon polarization component ( $\vec{\epsilon}_i$ ) is parallel to the scattering plane ( $\pi$ -polarization). The scattering plane is defined by wave vectors of the incident and the scattered photons. In this section, we present the photon polarization dependence of the RIXS spectra in  $\text{FeBO}_3$ .

2D plots in Fig. 3(b) and (d) show how the RIXS intensities change with  $\mathbf{Q}$ . First, we note that elastic line intensities in both cases reduce substantially as  $\mathbf{Q}$



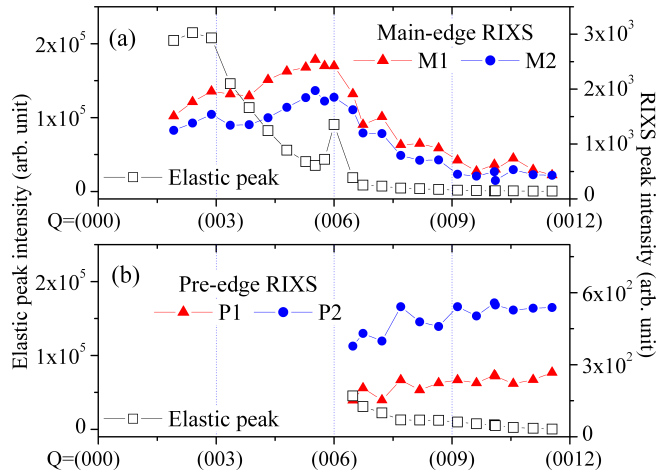


FIG. 4: Intensity of charge excitations measured as a function of momentum transfer  $Q$  in (a) main-edge and (b) pre-edge RIXS. Open square symbols denote the elastic peak intensities, while filled symbols denote the inelastic peak intensities. Increased elastic intensity at  $Q=(0\ 0\ 6)$  is due to the proximity to the Bragg reflection.

increases, especially, when  $2\theta$  approaches  $90^\circ$  ( $L \simeq 12$ ). This is related to the fact that the polarization dependence of the elastic (Thomson) scattering cross section is proportional to the scalar product  $\vec{\epsilon}_i \cdot \vec{\epsilon}_s$  of  $\vec{\epsilon}_i$  and scattered photon polarization ( $\vec{\epsilon}_s$ ).

The main-edge and the pre-edge RIXS spectra show quite different inelastic intensity changes with  $Q$ . In the case of the main-edge RIXS, the intensity of the charge excitations is more or less stable near  $Q=(0\ 0\ 6)$  but rapidly disappears for a higher  $Q$ , as shown in Fig. 3(b). On the other hand, the intensities of the charge excitations in the pre-edge RIXS do not show any dramatic  $Q$  dependence.

Figure 4(a) shows the peak intensity change with  $Q$  of the main-edge RIXS feature. The elastic intensity shows a rapid drop above  $Q=(0\ 0\ 3)$ . The large elastic peak intensity at  $Q=(0\ 0\ 6)$  corresponds to the first Bragg reflection. The inelastic intensities of M1 and M2 peaks start to decrease after  $Q=(0\ 0\ 6)$  and become quite small for higher  $Q$ . In contrast, Fig. 4(b) shows that the intensities of the P1 and P2 peaks are more or less stable over the whole  $Q$  range.

#### D. Temperature dependence

To study the temperature dependence, the main-edge and pre-edge RIXS spectra were measured at different crystal temperatures in the vicinity of the Néel point,  $T_N=348$  K. Figures 5(a) and (b) show the main-edge and pre-edge RIXS spectra, respectively, on the scale enlarged around the P1 peak. The measurements were performed at the momentum transfer  $Q=(0\ 0\ 9)$ . For a better comparison, the RIXS spectra measured at  $T = 300$  K are superimposed on the spectra measured at higher tem-

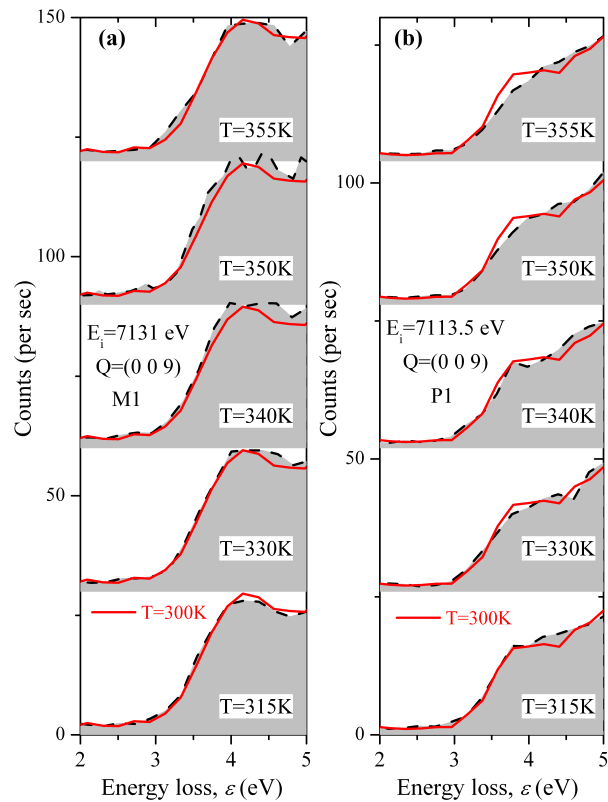


FIG. 5: (a) Main-edge RIXS ( $E_i=7131$  eV,  $Q=(0\ 0\ 9)$ ) and (b) pre-edge RIXS ( $E_i=7113.5$  eV,  $Q=(0\ 0\ 9)$ ) spectra measured at different crystal temperatures in the vicinity of the Néel transition temperature  $T_N=348$  K.

perature. No significant systematic change is observed for the main-edge RIXS spectra with temperature. The spectrum measured above  $T_N$  at temperature  $T = 355$  K matches well to the one measured at  $T = 300$  K. On the other hand, the pre-edge RIXS spectrum shows a noticeable change when crossing  $T_N$ . Above  $T_N$ , the P1 peak becomes broad, resulting in a decreased spectral intensity.

In optical spectroscopy, evidence has accumulated for the sensitivity of MH excitations to local magnetic correlations, that is, to the alignments of the nearest neighbor (NN) spins. For example,  $\text{LaMnO}_3$  is an *A*-type antiferromagnetic insulator, with a ferromagnetic coupling along the **b**-axis and an antiferromagnetic coupling along the **c**-axis. Upon magnetic ordering, the spectral intensity of the lowest energy excitation around 2 eV, which is associated with the MH excitation, increases for the **b**-axis but decreases for the **c**-axis.<sup>41</sup> Similar sensitivity of MH excitations to local magnetic correlations was reported in a recent RIXS study on a series of doped manganite systems.<sup>22</sup> It was shown that the low energy RIXS spectral intensity increases for FM nearest neighbor (NN) but decreases for paramagnetic (PM) NN. On the other hand, the spectral intensity of the CT excitations is known to be insensitive to local magnetic cor-

relations, because the oxygen  $2p$  states are completely filled. An often observed gradual temperature dependence of CT excitation spectral intensity is attributed to changes in the bond length or the orbital occupation. No RIXS studies have evidenced the sensitivity of the CT excitations to magnetic order. The different temperature dependences for MH and CT excitations have been exploited to distinguish between these two excitations in the optical spectroscopy.<sup>42</sup>

Using this analogy, one can suggest that no change in the main-edge RIXS spectra is another argument that charge excitations probed by this scattering process are CT excitations. The observed temperature dependence in the pre-edge RIXS spectra suggests that charge excitations probed by this scattering process are MH excitations. The temperature dependence can be understood in the strong crystal-field limit. As mentioned before, five  $d$  electrons in  $\text{FeBO}_3$  fill three-fold degenerate  $t_{2g}$  and two-fold degenerate  $e_g$  in the high-spin configuration. The Mott-Hubbard excitation in  $\text{FeBO}_3$  is the intersite charge transfer between two neighboring Fe ion sites resulting in  $d^4$  on one site and  $d^6$  on the other site. In the antiferromagnetic NN alignment, this transition occurs easily because the NN site has the unoccupied level with the same spin with the electron at the center site. On the other hand, in the ferromagnetic NN alignment, the electron at the center site cannot hop to the NN site because of the opposite spin state of the unoccupied level at the NN site. Therefore, the change in the antiferromagnetic NN alignment will be reflected in the MH excitation.

#### IV. DISCUSSION AND SUMMARY

In the previous section, we presented the Fe K edge RIXS spectra in  $\text{FeBO}_3$  measured under different conditions, as a function of incident photon energy, momentum transfer, photon polarization, and temperature. The pre-edge and main-edge RIXS reveal different types of charge excitations. The charge excitations probed by the main-edge RIXS show a typical  $E_i$  dependence observed in a number of previous RIXS studies in cuprates.<sup>14,25,34</sup> Two low-lying M1 and M2 peaks show the dispersion widths of 0.26 eV and 0.44 eV, respectively, and their intensities drop rapidly as  $|\mathbf{Q}|$  increases. These excitations turned out to be insensitive to the crystal temperature. On the contrary, the charge excitation revealed by the pre-edge RIXS does not show any dispersion and any intensity change with  $\mathbf{Q}$ . As the crystal temperature exceeds  $T_N$ , the P1 excitation with lowest energy broadens and decreases in intensity. The observed temperature dependence is directly related to local magnetic correlations. We attribute the main-edge and pre-edge RIXS excitations to CT and MH excitations, respectively. In the following, we discuss CT and MH excitations using molecular orbitals (MO) in the cluster model and multiplet calculation in the many-electron multiband model, respectively.

#### A. Charge-transfer excitation

The ground state of undistorted octahedral  $\text{Fe}^{3+}\text{O}_6$  of  $\text{FeBO}_3$  is described by filled non-bonding anionic ( $O\ 2p$ ) MO ( $a_{1g}(\sigma), t_{1g}(\pi), t_{1u}(\sigma), t_{1u}(\pi)$ , and  $t_{2u}(\pi)$ ), filled bonding cationic MO ( $t_{2g}(\pi)$  and  $e_g(\sigma)$ ), and unfilled anti-bonding  $3d$ -type MO ( $t_{2g}$  and  $e_g$ ).<sup>44</sup> The CT excitation arises at the transition from the anionic odd-parity MO ( $t_{1u}(\sigma), t_{1u}(\pi)$ , and  $t_{2u}(\pi)$ ) into the even-parity  $3d$ -type MO ( $t_{2g}$  and  $e_g$ ). Six CT excitations are allowed in the frame work of this model. Among them, there are three strong dipole CT transitions between MO states with the same bonding symmetry:  $t_{2u}(\pi) \rightarrow t_{2g}$ ,  $t_{1u}(\pi) \rightarrow t_{2g}$ , and  $t_{1u}(\sigma) \rightarrow e_g$ .

Let us analyse the structure of the  $t_{1u}(\sigma), t_{1u}(\pi)$ , and  $t_{2u}(\pi)$  energy states. The energy  $E(t_{1u}(\sigma))$  of  $t_{1u}(\sigma)$  is lower than  $E(t_{1u}(\pi))$  and  $E(t_{2u}(\pi))$  due to its larger Madelung potential. Optical study suggests that  $E(t_{2u}(\pi))$  in  $\text{FeBO}_3$  is higher than  $E(t_{1u}(\pi))$ .<sup>45</sup> It is also known that  $E(t_{2u}(\pi))$  and  $E(t_{1u}(\pi))$  are 2.2 eV and 1.2 eV higher, respectively, than  $E(t_{1u}(\sigma))$ .<sup>43,44</sup>

In the MO model, therefore, the lowest CT excitation is the transition from the highest occupied MO to the lowest unoccupied MO, that is,  $t_{2u}(\pi) \rightarrow t_{2g}$ . The next one is  $t_{1u}(\pi) \rightarrow t_{2g}$ . If we use the literature values mentioned above, the energy difference between these two CT excitations is 1.2 eV. This value is in agreement with the observed mean energy difference between M1 and M2, which is about 1.13 eV. Therefore, it is plausible to assign M1 and M2 excitations revealed in the main-edge RIXS to  $t_{2u}(\pi) \rightarrow t_{2g}$  and  $t_{1u}(\pi) \rightarrow t_{2g}$ , respectively.

The highest CT excitation in this model is  $t_{1u}(\sigma) \rightarrow e_g$ . Assuming that  $E(t_{2u}(\pi)) - E(t_{1u}(\sigma)) = 2.2$  eV and  $E(e_g) - E(t_{2g}) \equiv 10Dq = 1.4$  eV, we can estimate that its energy is 3.6 eV higher than the energy of the lowest  $t_{2u}(\pi) \rightarrow t_{2g}$  transition. This energy difference of 3.6 eV has to be comparable with the observed energy difference between the M1 and M3 excitations (4.31 eV). The discrepancy can be attributed to some effects, such as

TABLE I: Peaks in the measured main-edge and pre-edge RIXS spectra and their assignments in the framework of MO in the cluster model, and multiplet calculation in the many-electron multiband model as in Ref. 10, respectively. The peak energies are measured at  $\mathbf{Q}=(0\ 0\ 6)$ . Energies in parenthesis are literature values (Ref. 43).

Peak	Assigned transition	Energy (eV)
Main-edge RIXS		
M1	$t_{2u}(\pi) \rightarrow t_{2g}$	3.81
M2	$t_{1u}(\pi) \rightarrow t_{2g}$	4.94 (5.01)
M3 <sup>a</sup>	$t_{1u}(\sigma) \rightarrow e_g$	8.14 (7.41)
Pre-edge RIXS		
P1	$d^5 : {}^5A_{1g} + d^5 : {}^5A_{1g} \rightarrow$	
P2	$d^6 : {}^5T_{2g} + d^4 : {}^5E_g$	3.96
P3	$d^6 : {}^5E_g + d^4 : {}^5E_g$	5.85 (5.36)
P3	$d^6 : {}^1A_g + d^4 : {}^1T_{2g}$	8.71 (8.62)

<sup>a</sup>See the text for another plausible assignment.

an octahedral distortion, which are not included in our cluster model. Therefore, we can assign the M3 peak to the  $t_{1u}(\sigma) \rightarrow e_g$  transition. Peak assignments are summarized in Table I.

The other plausible interpretation of the M3 excitation is due to MO excitation from bonding to anti-bonding MO states. Taking into account that bonding states are lower in energy than non bonding states, this MO excitation can explain the larger energy separation of M1 and M3. This type of MO excitation has been found in a number of cuprates.<sup>46</sup> It resonates at a higher incident photon energy  $E_i$ , and its peak width is much larger than lower energy CT excitations. Actually the  $E_i$  dependence in Figs. 2(c) and (d) shows that M3 resonates at about 4 eV higher  $E_i$  than M1 and M2. The peak width of M3 is much broader compared with M1 and M2 (see Fig. 2(e)).

We have observed that M1 and M2 peaks show the dispersion widths of 0.26 eV and 0.44 eV, respectively. To fully understand this momentum transfer dependence, more advanced calculations are needed beyond the local cluster model. This would be very important for better understanding the electronic structure of FeBO<sub>3</sub>.

## B. Mott-Hubbard excitation

We will use the many-electron multiband model by Ovchinnikov and Zabluda to analyze MH excitation in FeBO<sub>3</sub>.<sup>10,47</sup> In this model, the Hamiltonian of the system is written as

$$H = \sum_{\lambda,\sigma} (\varepsilon_\lambda n_{\lambda\sigma} + \frac{U_\lambda}{2} n_{\lambda\sigma} n_{\lambda\bar{\sigma}}) + \sum_{\substack{\lambda,\lambda' \\ (\lambda \neq \lambda')}} \sum_{\sigma,\sigma'} (V_{\lambda\lambda'} n_{\lambda\sigma} n_{\lambda'\sigma'} - J_{\lambda\lambda'} a_{\lambda\sigma}^\dagger a_{\lambda\sigma'} a_{\lambda'\sigma'}^\dagger a_{\lambda'\sigma}). \quad (1)$$

Here  $\lambda$  and  $\sigma$  are the orbital and the spin indices,  $a_{\lambda\sigma}$  ( $a_{\lambda\sigma}^\dagger$ ) is the creation (annihilation) operator of  $d$  electrons with the spin  $\sigma$ , and  $n_{\lambda\sigma} = a_{\lambda\sigma}^\dagger a_{\lambda\sigma}$ . The quantity  $\varepsilon_\lambda$  is the atomic  $3d$  level energy that may take the values of  $\varepsilon(t_{2g}) = \varepsilon_d - 0.4 \times (10Dq)$  and  $\varepsilon(e_g) = \varepsilon_d + 0.6 \times (10Dq)$ . Coulomb intraorbital repulsion energy  $U_\lambda$  is nonzero when the  $3d$  electron occupies the same orbital with the different spin. Coulomb interorbital repulsion energy  $V_{\lambda\lambda'}$  is nonzero when a  $3d$  electron occupies a different orbital. Hund exchange energy  $J_{\lambda\lambda'}$  is nonzero when a  $3d$  electron occupies a different orbital with the same spin. Neglecting the orbital dependence, these three energies are related by  $U = 2V + J$ . Note that this is an atomic model, ignoring  $3d$  spin-orbit interaction and inter atomic exchange.

The ground-state crystalline term of FeBO<sub>3</sub> is  ${}^6A_{1g}$ . Its energy  $E(d^5: {}^6A_{1g})$  is equal to  $3\varepsilon(t_{2g}) + 2\varepsilon(e_g) + 10V - 10J = 5\varepsilon_d + 10V - 10J$ . The lowest  $d^4$  configuration corresponds to occupied three  $t_{2g}$  and one  $e_g$  states in the high spin configuration in which the

crystalline term is  ${}^5E_g$ . Its energy  $E(d^4: {}^5E_g)$  is equal to  $3\varepsilon(t_{2g}) + \varepsilon(e_g) + 6V - 6J = 4\varepsilon_d - 0.6 \times 10Dq + 6V - 6J$ . The lowest  $d^6$  configuration corresponds to occupied four  $t_{2g}$  and two  $e_g$  in the high spin configuration in which the crystalline term is  ${}^5T_{2g}$ . Its energy  $E(d^6: {}^5T_{2g})$  is equal to  $4\varepsilon(t_{2g}) + 2\varepsilon(e_g) + U + 14V - 10J = 6\varepsilon_d - 0.4 \times 10Dq + U + 14V - 10J$ . Now we can calculate the lowest MH excitation energy  $U_G = E(d^6: {}^5T_{2g}) + E(d^4: {}^5E_g) - 2E(d^5: {}^6A_{1g}) = U + 4J - 10Dq$ .

Higher MH excitations arise from excited  $d^4$  and  $d^6$  configurations. Crystalline terms of excited  $d^4$  configurations are  ${}^3T_{1g}$  and  ${}^1T_{2g}$  in the order of increasing energy, while those of excited  $d^6$  configurations are  ${}^5E_g$ ,  ${}^1A_{1g}$ ,  ${}^3T_{1g}$  and  ${}^3T_{2g}$ . Considering the spin-selection rule, higher MH excitations are  $E(d^6: {}^5E_g) + E(d^4: {}^5E_g) - 2E(d^5: {}^6A_{1g}) = U_G + 10Dq$  and  $E(d^6: {}^1A_{1g}) + E(d^4: {}^1T_{2g}) - 2E(d^5: {}^6A_{1g}) = U_G + 2U - 2V + 6J - 2 \times 10Dq$  in the order of increasing energy.

We assign the P1 peak in the pre-edge RIXS spectra to the lowest MH excitation and obtain  $U_G = U + 4J - 10Dq = 3.96$  eV. The literature values for  $J$  are spread from 0.35 eV to 1 eV.<sup>10,12,47</sup> Based on optical studies, Ovchinnikov and Zabluda<sup>10</sup> obtained  $U = 2.97$  eV using  $J = 0.7$  eV and  $10Dq = 1.57$  eV. In our case, we are measuring  $10Dq = 1.4$  eV (see Fig. 2(b)) and obtain  $U = 2.56$  eV assuming  $J = 0.7$  eV.

The second MH excitation energy is equal to 5.36 eV, which is  $10Dq = 1.4$  eV higher than the lowest one. We observe that the mean energy difference between P1 and P2 is about 1.85 eV. We assign the P2 peak to the second MH excitation:  $(d^5: {}^6A_{1g}) + (d^5: {}^6A_{1g}) \rightarrow (d^6: {}^5E_g) + (d^4: {}^5E_g)$ . The somewhat large discrepancy in energy can be attributed to various effects, such as  $3d$  spin-orbit interaction and inter atomic exchange, which are not included in the model. In addition, the energy estimation is based on the local multiplet model where the inter site excitation state is a simple product of two single site states and inter site mixing is not included. In this regard, more refined model calculations are desirable. In the case of the third MH excitation, the calculated energy equals to 8.62 eV. Since the energy of the P3 excitation is 8.71 eV, we can assign the P3 excitation to the third MH excitation:  $(d^5: {}^6A_{1g}) + (d^5: {}^6A_{1g}) \rightarrow (d^6: {}^1A_{1g}) + (d^4: {}^1T_{2g})$ . Peak assignments are summarized in Table I.

## C. Electronic structure in FeBO<sub>3</sub>

We have assigned all observed peaks in the measured RIXS spectra using molecular orbitals (MO) in the cluster model and multiplet calculation in the many-electron multiband model. Using these assignments, we can derive the electronic structure around the chemical potential ( $\mu$ ) in FeBO<sub>3</sub>. The lowest UHB energy is  $E(d^6: {}^5T_{2g}) - E(d^5: {}^6A_{1g}) = \varepsilon_d - 0.4 \times 10Dq + U + V = \varepsilon_d + 5.72$  eV and the highest LHB energy is  $E(d^4: {}^5E_g) - E(d^5: {}^6A_{1g}) = -\varepsilon_d - 0.6 \times 10Dq - 4V + 4V = -\varepsilon_d - 1.76$  eV, resulting in  $U_c = 3.96$  eV. On the other hand, when  $-\varepsilon_p$  is introduced



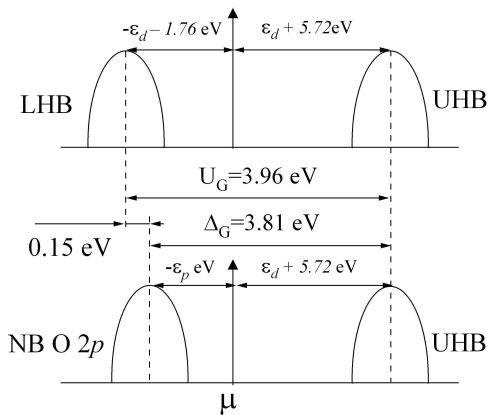


FIG. 6: Schematic of electronic structure around the chemical potential ( $\mu$ ) in  $\text{FeBO}_3$ . Energies are in the unit of eV, based on the results of the presented RIXS measurements.

to describe the non bonding (NB)  $O\ 2p$  state relative to  $\mu$ , the lowest CT energy is  $\varepsilon_d + 5.72 - \varepsilon_p$  eV, resulting in  $\Delta_G = 3.81$  eV.

The schematic in Fig. 6 presents the electronic structure in  $\text{FeBO}_3$  around  $\mu$  based on our RIXS studies. Our experimental results support the conclusion that  $\text{FeBO}_3$  is a CT insulator, as found by Ovchinnikov and Zabluda<sup>10</sup> based on optical absorption and photoemission spectroscopy studies. However, the values for the energy separation between NB  $O\ 2p$  and LHB are quite different: 0.15 eV in the present study, and 1.4 eV in the study reported by Ovchinnikov and Zabluda. We believe that our result is more accurate because it was obtained, model independent using the same spectroscopy to probe both CT and MH excitations.

## V. SUMMARY

In this study, we report the first successful resonant inelastic x-ray scattering (RIXS) measurement at the K absorption edge of Fe. We observe qualitatively different RIXS excitations associated with the main-edge and pre-edge absorption phenomena. These two types of excitations have different incident energy, polarization, and

momentum dependence. We interpret the main-edge and pre-edge RIXS excitations as charge-transfer and Mott-Hubbard excitations, respectively. We assign and discuss CT and MH excitations using molecular orbitals (MO) in the cluster model and multiplet calculation in the many-electron multiband model, respectively. The present study demonstrates the utility of  $K$  edge RIXS as a simultaneous probe of charge-transfer and Mott-Hubbard excitations in transition metal compounds. Novel phenomena of the insulator-semiconductor transition and the collapse of the magnetic moment have been observed recently in  $\text{FeBO}_3$  under pressure.<sup>5-7</sup> For a detailed understanding of these phenomena, it is essential to know charge-transfer energy, crystal-field splitting  $10Dq$ , and Coulomb repulsion  $U$ . We have demonstrated that  $K$  edge RIXS can be used to measure these quantities directly.  $K$  edge RIXS, being a hard x-ray bulk-sensitive probe, can be applied for high-pressure studies. It would be very appealing in the next step to use these techniques to study the pressure-induced electronic and magnetic property changes in  $\text{FeBO}_3$ .

## Acknowledgments

Yu. Sh. acknowledges the longstanding effort of his colleagues from the IXS Collaborative Design Team in building MERIX instrument at the XOR-IXS 30-ID beamline at the APS, in particular of John Hill, Scott Coburn (BNL), Clement Burns (WMU), Ercan Alp, Thomas Toellner, and Harald Sinn (APS). He is also indebted to Ruben Khachatryan (APS), Michael Wiczorek (APS), and Ayman Said (APS) for the help in manufacturing the Ge(620) analyzer. Peter Siddons (BNL) is acknowledged for building the microstrip detector for the MERIX spectrometer. The help of the XOR-IXS 30-ID beamline personnel at the Advanced Photon Source: Tim Roberts, Ayman Said, Mary Upton is greatly appreciated. Use of the Advanced Photon Source was supported by the U. S. DOE, Office of Science, Office of Basic Energy Sciences, under Contract No. DE-AC02-06CH11357.

\* Electronic address: jhkim@aps.anl.gov

† Electronic address: shvydko@aps.anl.gov

<sup>1</sup> R. Diehl, W. Jantz, B. J. Nöläng, and W. Wettling, *Curr. Top. Mater. Sci.* **11**, 241 (1984).

<sup>2</sup> A. J. Kurtzig, R. Wolfe, R. C. Lecraw, and J. W. Nielsen, *Appl. Phys. Lett.* **14**, 350 (1969).

<sup>3</sup> R. Wolfe, A. J. Kurtzig, and R. C. Lecraw, *J. Appl. Phys.* **41**, 1218 (1970).

<sup>4</sup> I. A. Troyan, A. G. Gavriliuk, V. A. Sarkisyan, I. S. Lyubutin, R. Ruffer, O. Leupold, A. Barla, B. Doyle, and A. I. Chumakov, *JETP Lett.* **74**, 2001 (2001).

<sup>5</sup> V. A. Sarkisyan, I. A. Troyan, M. S. Lyubutin, A. G. Gavrilyuk, and A. F. Kashuba, *JETP Lett.* **76**, 664 (2002).

<sup>6</sup> I. A. Troyan, M. I. Eremets, A. G. Gavrilyuk, I. S. Lyubutin, and V. A. Sarkisyan, *JETP Lett.* **78**, 13 (2003).

<sup>7</sup> A. G. Gavriliuk, I. A. Trojan, S. G. Ovchinnikov, I. S. Lyubutin, and V. A. Sarkisyan, *JETP Lett.* **99**, 566 (2004).

<sup>8</sup> A. G. Gavriliuk, I. A. Trojan, I. S. Lyubutin, S. G. Ovchinnikov, and V. A. Sarkisyan, *JETP Lett.* **100**, 688 (2005).

<sup>9</sup> I. S. Lyubutin, S. G. Ovchinnikov, A. G. Gavriliuk, and V. V. Struzhkin, *Phys. Rev. B* **79**, 085125 (2009).

<sup>10</sup> S. G. Ovchinnikov and V. N. Zabluda, *JETP Lett.* **98**, 135

- (2004).
- <sup>11</sup> A. V. Postnikov, S. Bartkowski, M. Neumann, R. A. Rupp, E. Z. Kurmaev, S. N. Shamin, and V. V. Fedorenko, *Phys. Rev. B* **50**, 14849 (1994).
  - <sup>12</sup> S. Shang, Y. Wang, Z.-K. Liu, C.-E. Yang, and S. Yin, *Appl. Phys. Lett.* **91**, 253115 (2007).
  - <sup>13</sup> J. Zaanen, G. A. Sawatzky, and J. W. Allen, *Phys. Rev. Lett.* **55**, 418 (1985).
  - <sup>14</sup> P. Abbamonte, C. A. Burns, E. D. Isaacs, P. M. Platzman, L. L. Miller, S. W. Cheong, and M. V. Klein, *Phys. Rev. Lett.* **83**, 860 (1999).
  - <sup>15</sup> M. Z. Hasan, E. D. Isaacs, Z.-X. Shen, L. L. Miller, K. Tsutsui, T. Tohyama, and S. Maekawa, *Science* **288**, 1811 (2000).
  - <sup>16</sup> Y. J. Kim, J. P. Hill, C. A. Burns, S. Wakimoto, R. J. Birgeneau, D. Casa, T. Gog, and C. T. Venkataraman, *Phys. Rev. Lett.* **89**, 177003 (2002).
  - <sup>17</sup> Y.-J. Kim, J. P. Hill, H. Benthien, F. H. L. Essler, E. Jeckelmann, H. S. Choi, T. W. Noh, N. Motoyama, K. M. Kojima, S. Uchida, D. Casa, and T. Gog, *Phys. Rev. Lett.* **92**, 137402 (2004).
  - <sup>18</sup> K. Ishii, K. Tsutsui, Y. Endoh, T. Tohyama, K. Kuzushita, T. Inami, K. Ohwada, S. Maekawa, T. Masui, S. Tajima, Y. Murakami, and J. Mizuki, *Phys. Rev. Lett.* **94**, 187002 (2005).
  - <sup>19</sup> S. Suga, S. Imada, A. Higashiya, A. Shigemoto, S. Kasai, M. Sing, H. Fujiwara, A. Sekiyama, A. Yamasaki, C. Kim, T. Nomura, J. Igarashi, M. Yabashi, and T. Ishikawa, *Phys. Rev. B* **72**, 081101(R) (2005).
  - <sup>20</sup> L. Lu, X. Zhao, J. N. Hancock, G. Chabot-Couture, N. Kaneko, O. P. Vajk, G. Yu, S. Grenier, Y. J. Kim, D. Casa, T. Gog, and M. Greven, *Phys. Rev. Lett.* **95**, 217003 (2005).
  - <sup>21</sup> T. Inami, T. Fukuda, J. Mizuki, S. Ishihara, H. Kondo, H. Nakao, T. Matsumura, K. Hirota, Y. Murakami, S. Maekawa, and Y. Endoh, *Phys. Rev. B* **67**, 045108 (2003).
  - <sup>22</sup> S. Grenier, J. P. Hill, V. Kiryukhin, W. Ku, Y.-J. Kim, K. J. Thomas, S.-W. Cheong, Y. Tokura, Y. Tomioka, D. Casa, and T. Gog, *Phys. Rev. Lett.* **94**, 047203 (2005).
  - <sup>23</sup> E. Collart, A. Shukla, J.-P. Rueff, P. Leininger, H. Ishii, I. Jarrige, Y. Q. Cai, S.-W. Cheong, and G. Dhalenne, *Phys. Rev. Lett.* **96**, 157004 (2006).
  - <sup>24</sup> S. Wakimoto, H. Kimura, K. Ishii, K. Ikeuchi, T. Adachi, M. Fujita, K. Kakurai, Y. Koike, J. Mizuki, Y. Noda, K. Yamada, A. H. Said, and Y. Shvyd'ko, *Phys. Rev. Lett.* **102**, 157001 (2009).
  - <sup>25</sup> Y.-J. Kim, J. P. Hill, S. Wakimoto, R. J. Birgeneau, F. C. Chou, N. Motoyama, K. M. Kojima, S. Uchida, D. Casa, and T. Gog, *Phys. Rev. B* **76**, 155116 (2007).
  - <sup>26</sup> J. Kim, D. S. Ellis, H. Zhang, Y.-J. Kim, J. P. Hill, F. C. Chou, T. Gog, and D. Casa, *Phys. Rev. B* **79**, 094525 (2009).
  - <sup>27</sup> P. Kuiper, J.-H. Guo, C. Sathe, L.-C. Duda, J. Nordgren, J. J. M. Poethuizen, F. M. F. de Groot, and G. A. Sawatzky, *Phys. Rev. Lett.* **80**, 5204 (1998).
  - <sup>28</sup> G. Ghiringhelli, N. B. Brookes, E. Annese, H. Berger, C. Dallera, M. Grioni, L. Perfetti, A. Tagliaferri, and L. Braicovich, *Phys. Rev. Lett.* **92**, 117406 (2004).
  - <sup>29</sup> W. Schülke, *Electron dynamics by inelastic X-ray scattering*, Oxford Series on Synchrotron Radiation (Oxford University Press, 2007, Oxford; New York, 2007).
  - <sup>30</sup> T. Toellner, Argonne National Laboratory, unpublished.
  - <sup>31</sup> S. Huotari, G. Vanko, F. Albergamo, C. Ponchut, H. Graafsma, C. Henriquet, R. Verbeni, and G. Monaco, *J. Synch. Rad.* **12**, 467 (2005).
  - <sup>32</sup> M. Kotrbova, S. Kadeckova, J. Novak, J. Bradler, G. V. Smirnov, and Y. V. Shvyd'ko, *Journal of Crystal Growth* **71**, 607 (1985).
  - <sup>33</sup> T. E. Westre, P. Kennepohl, J. G. DeWitt, B. Hedman, K. O. Hodgson, and E. I. Solomon, *J. Am. Chem. Soc.* **119**, 6297 (1997).
  - <sup>34</sup> L. Lu, J. N. Hancock, G. Chabot-Couture, K. Ishii, O. P. Vajk, G. Yu, J. Mizuki, D. Casa, T. Gog, and M. Greven, *Phys. Rev. B* **74**, 224509 (2006).
  - <sup>35</sup> P. M. Platzman and E. D. Isaacs, *Phys. Rev. B* **57**, 11107 (1998).
  - <sup>36</sup> G. Ghiringhelli, M. Matsubara, C. Dallera, F. Fracassi, R. Gusmeroli, A. Piazzalunga, A. Tagliaferri, N. B. Brookes, A. Kotani, and L. Braicovich, *J. Phys.: Condens. Matter* **17**, 5397 (2005).
  - <sup>37</sup> K. Tsutsui, T. Tohyama, and S. Maekawa, *Phys. Rev. Lett.* **91**, 117001 (2003).
  - <sup>38</sup> K. Ishii, K. Tsutsui, T. Tohyama, T. Inami, J. Mizuki, Y. Murakami, Y. Endoh, S. Maekawa, K. Kudo, Y. Koike, and K. Kumagai, *Phys. Rev. B* **76**, 045124 (2007).
  - <sup>39</sup> D. S. Ellis, J. P. Hill, S. Wakimoto, R. J. Birgeneau, D. Casa, T. Gog, and Y.-J. Kim, *Phys. Rev. B* **77**, 060501(R) (2008).
  - <sup>40</sup> K. Ishii, T. Inami, K. Ohwada, K. Kuzushita, J. Mizuki, Y. Murakami, S. Ishihara, Y. Endoh, S. Maekawa, K. Hirota, and Y. Moritomo, *Phys. Rev. B* **70**, 224437 (2004).
  - <sup>41</sup> N. N. Kovaleva, A. V. Boris, C. Bernhard, A. Kulakov, A. Pimenov, A. M. Balbashov, G. Khaliullin, and B. Keimer, *Phys. Rev. Lett.* **93**, 147204 (2004).
  - <sup>42</sup> A. Gössling, M. W. Haverkort, M. Benomar, H. Wu, D. Senff, T. Möller, M. Braden, J. A. Mydosh, and M. Grüninger, *Phys. Rev. B* **77**, 035109 (2008).
  - <sup>43</sup> A. I. Liechtenshtein, A. S. Moskvina, and V. A. Gubanov, *Sov. Phys. Solid State* **24**, 2049 (1982).
  - <sup>44</sup> R. V. Pisarev, A. S. Moskvina, A. M. Kalashnikova, and T. Rasing, *Phys. Rev. B* **79**, 235128 (2009).
  - <sup>45</sup> P. A. Markovin, A. M. Kalashnikova, R. V. Pisarev, and T. Rasing, *JETP Lett.* **86**, 712 (2007).
  - <sup>46</sup> Y.-J. Kim, J. P. Hill, G. D. Gu, F. C. Chou, S. Wakimoto, R. J. Birgeneau, S. Komiya, Y. Ando, N. Motoyama, K. M. Kojima, et al., *Phys. Rev. B* **70**, 205128 (2004).
  - <sup>47</sup> S. G. Ovchinnikov, *JETP Lett.* **77**, 12 (2003).